Planetary Period Oscillations in Saturn's Magnetosphere: Comparison of Magnetic and SKR Modulation Periods and Phases During Northern Summer to the End of the Cassini Mission

G. Provan, L. Lamy, S. Cowley, E. Bunce

JGR Space Physics

RESEARCH ARTICLE
10.1029/2018JA026079

Planetary Period Oscillations in Saturn's Magnetosphere: Comparison of Magnetic and SKR Modulation Periods and Phases During Northern Summer to the End of the Cassini Mission

G. Provan[1], L. Lamy[2], S. W. H. Cowley[1], and E. J. Bunce[1]

[1]Department of Physics and Astronomy, University of Leicester, Leicester, UK, [2]LESIA, Observatoire de Paris, PSL Research University, CNRS, Sorbonne Universités, UPMC Université Paris 06, Université Paris Diderot, Sorbonne Paris Cité, Meudon, France

Key Points:

- Magnetic and SKR periods are near constant at 10.79/10.68 hr (±0.01 hr) for northern/southern PPOs during 2016–2017, agreeing to within ~ ±15 s
- Northern/southern upward PPO currents are centered postdawn at related SKR maxima as for other mission intervals with dawnside apoapsides
- Southern hemisphere SKR emissions are dual modulated at the northern period approximately in phase with the northern emissions

Correspondence to:
G. Provan,
gp31@le.ac.uk

Citation:
Provan, G., Lamy, L., Cowley, S. W. H., & Bunce, E. J. (2019). Planetary period oscillations in Saturn's magnetosphere: Comparison of magnetic and SKR modulation periods and phases during northern summer to the end of the Cassini mission. *Journal of Geophysical Research: Space Physics*, *124*, 1157–1172. https://doi.org/10.1029/2018JA026079

Received 12 SEP 2018
Accepted 21 JAN 2019
Accepted article online 1 FEB 2019
Published online 23 FEB 2019

Abstract We compare periods and phases of Saturn planetary period oscillations determined from Cassini magnetic field and Saturn kilometric radiation (SKR) data from the beginning of 2016 to the end of mission in mid-September 2017, encompassing northern summer solstice in May 2017. Both data sets show that the periods are almost unchanging, varying by only ~ ±0.01 hr about 10.79 hr for the northern system and 10.68 hr for the southern system, close to values attained by mid-2015 after period coalescence between mid-2013 and mid-2014. The mean absolute differences between the magnetic and SKR periods are ~0.0036 hr (~13 s), consistent with estimated magnetic measurement uncertainties, while the overall mean difference is less than 0.001 hr (~2–3 s), at the limit of resolution. The relative phasing between magnetic and SKR modulations is correspondingly near constant and such that the equatorial planetary period oscillation fields of the northern/southern systems point radially outward near-oppositely at ~14.3/2.5 hr local time at corresponding SKR maxima, with upward planetary period oscillation currents located ~2 hr postdawn for both systems, consistent with previous intervals having dawnside spacecraft apoapsides. Southern SKR emissions are found to be significantly dual modulated at both southern and northern periods in data limited to lie well within the southern shadow zone of the northern sources. These northern period modulations are shown to be approximately in phase with those in the northern emissions, consistent with a recent suggestion that bidirectional auroral electron acceleration may generate in phase SKR emissions in both hemispheres.

1. Introduction

Despite the perfect axisymmetry of Saturn's internally generated external magnetic field, within measurement uncertainty (Burton et al., 2010; Dougherty et al., 2018), modulations at approximations to Saturn's rotation period, termed "planetary period oscillations" (PPOs), have nevertheless been found to be ubiquitously present in magnetospheric plasma properties, energetic neutral atom emissions, plasma waves, magnetic fields, current systems and boundaries, as well as in auroral ultraviolet (UV), infrared, and radio emissions (see review by Carbary and Mitchell (2013), and references therein). Analyses of these modulations have pointed to the PPO sources being located in the two polar thermospheres/ionospheres, associated with rotating twin-vortex flows (Cowley et al., 2016; Hunt et al., 2014, 2015; Jia et al., 2012; Jia & Kivelson, 2012; Smith, 2006; Smith et al., 2016). Observations of the modulated radio emissions, specifically of Saturn kilometric radiation (SKR) generated by accelerated auroral electrons on field lines located around Saturn's auroral oval (Lamy, 2011; Lamy et al., 2009), have allowed the possibility of near-continuous remote monitoring of the PPO properties. These observations have shown that the periods associated with the two polar hemispheres are in general slightly different, varying by up to ~ ±1% about ~10.7 hr over Saturn's seasons (Fischer et al., 2015; Galopeau & Lecacheux, 2000; Gurnett et al., 2005, 2009, 2010, 2011; Kurth et al., 2008; Lamy, 2011, 2017; Lecacheux et al., 1997; Ye et al., 2016).

Arrival of the Cassini spacecraft at Saturn in July 2004 has also allowed near-continuous determination of PPO properties from in situ magnetic field data, with results being reported in a series of papers to the end of mission in September 2017 (Andrews et al., 2008, 2012; Provan et al., 2013, 2016, 2018). It is then evidently important to compare the results obtained from the independent radio emission and magnetic field

measurements, with the outcome of such comparisons being reported to date in papers covering data obtained to the end of 2015 (Andrews, Coates, et al., 2010; Provan et al., 2014, 2016). In general, the results show close levels of correspondence, although some intervals with systematic differences in period of a few tens of seconds or less have been noted, attributed to changes in spacecraft orbit which result in the observed SKR emissions responding to sources at differing local times (LTs) around the auroral oval (e.g., Andrews et al., 2011; Provan et al., 2014). These effects are a consequence of the conical beaming of the emissions about the auroral field lines, which for near-equatorial observations, for example, restricts the view of SKR sources to narrow segments of the auroral oval centered ~4 hr LT either side of the observing point (Lamy, Zarka, Cecconi, Prangé, et al., 2008; Lamy et al., 2009). A few instances of more significant discrepancy have also been discussed, much of which appears to be associated with uncertainties in data interpretation (Cowley & Provan, 2015, 2016; Fischer et al., 2014, 2015; Provan et al., 2016). Discrepancies could arise, for example, due to uncertainties in the number of whole cycles occurring between orbit to orbit magnetic phase determinations under conditions where the orbit period is long and the PPO period rapidly changing (see section 2.3), and to the hemispheric identification of northern and southern modulations in dual modulated SKR data (sections 2.4 and 4). Although some differences in results can thus arise from limitations in both data and analysis methods, we assert that in principle the periods associated with the magnetic and SKR phenomena cannot actually be different due to their mutual connection with the rotating current systems that both produce the magnetic perturbations and also drive the electron acceleration responsible for the SKR emission.

In this report we complete the comparative studies cited above by examining the relationship between PPO properties from the start of 2016 to the end of the Cassini mission in September 2017 derived independently from the magnetic field and SKR data by Provan et al. (2018) and Lamy (2017), respectively. This interval is of particular significance since the final sequence of ~40 F ring and proximal orbits of the Cassini mission starting in late 2016 have newly allowed repeated near-periapsis measurements in magnetospheric regimes not previously accessed (Dougherty et al., 2018; Hunt, Provan, Bunce, et al., 2018; Hunt, Provan, Cowley, et al., 2018), in particular on and inside inner ring-crossing field lines. Determination of the PPO properties in these regions requires secure knowledge of the period and phase of the PPO oscillations derived from measurements obtained at larger distances on these orbits, as investigated here.

2. PPO Current System, Data Interval, and Analysis Procedures

2.1. Nature of the PPO Current System

We begin by outlining in Figure 1 the basic nature of the PPO phenomenon that has emerged from previous studies, on which the discussion here is based (taken from Provan et al. (2018)). Figures 1a–1c refer to the northern PPO system and Figures 1d–1f to the southern system, where the red lines indicate the atmospheric/ionospheric flows taken to drive the PPOs, the blue lines and symbols the perturbation magnetic fields, and the green lines and symbols the related current system. Figures 1a and 1d show views looking down on the two polar ionospheres from the north, "through" the planet in the case of the southern hemisphere in Figure 1d, displaying the two magnetic phase/longitude systems $\Psi_{N,\,S}$ that define azimuthal position with respect to the northern (N) and southern (S) systems. At a fixed spatial position these phases monotonically increase with time as the systems rotate in the sense of planetary rotation at their individual periods, by 360° for a full turn. Figures 1b and 1e show the form of the principal current systems in the 90°–270° $\Psi_{N,\,S}$ meridian plane, in which the main field-aligned currents (thicker green lines) close partly in the magnetosphere and partly in the opposite ionosphere (Bradley et al., 2018; Hunt et al., 2014, 2015). The black lines indicate the near axisymmetric background field. Auroral phenomena are expected to be modulated as the field-aligned current systems rotate, superposed on quasi-steady currents associated with plasma subcorotation, with maxima occurring where the PPO current is directed upward out of the ionosphere, requiring downward acceleration of electrons, near $\Psi_N = 90^\circ$ in the northern hemisphere and $\Psi_S = 270^\circ$ in the southern. Figures 1c and 1f show the principal perturbation fields in the 0°–180° $\Psi_{N,\,S}$ meridian plane, consisting of a rotating quasi-uniform field in the equatorial region, which closes principally over each corresponding pole in the form of a rotating transverse dipole field (Andrews, Cowley, et al., 2010; Andrews et al., 2012; Hunt et al., 2015; Provan et al., 2009, 2011).

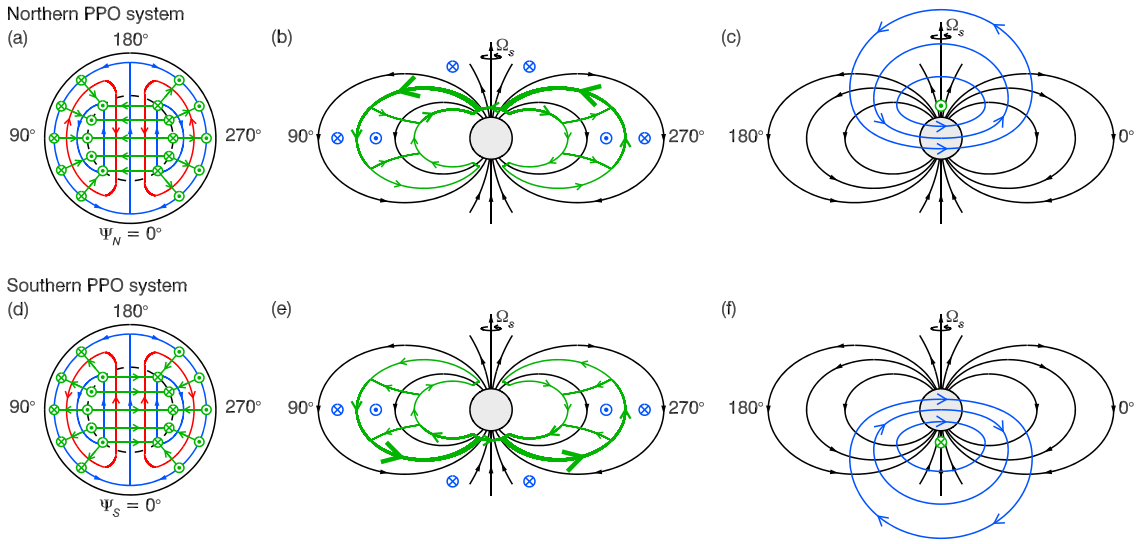

Figure 1. Sketches showing the form of the PPO-related perturbation fields and currents in Saturn's magnetosphere as discerned from Cassini studies, where Figures 1a–1c refer to the northern system and Figures 1d–1f to the southern system. Red lines indicate atmospheric/ionospheric flows, green lines and symbols PPO-related currents, and blue lines and symbols PPO perturbation magnetic fields. Circled dots and crosses indicate vectors pointing out of and into the plane of the diagram, respectively. Figures 1a and 1d show the views of the polar ionospheres from the north, looking "through" the planet in Figure 1d. These also show the PPO phases $\Psi_{N,\,S}$ employed to define azimuthal position with respect to these systems. Figures 1b and 1e show the currents and fields in the 90°–270° $\Psi_{N,\,S}$ meridian plane, where the black lines indicate the near axisymmetric planetary magnetic field. Figures 1c and 1f show the perturbation fields in the 0°–180° $\Psi_{N,\,S}$ meridian plane (from Provan et al., 2018).

2.2. Data Interval

The data interval examined here spans from the beginning of 2016 to the end of the Cassini mission on 15 September 2017, thus interfacing with the related results reported by Provan et al. (2016) to the end of 2015. As is evident from the form of the field perturbations indicated in Figure 1, consisting of a rotating quasi-uniform field in the equatorial region and a rotating quasi-dipolar field in the polar regions, the nature of the magnetic perturbations available for analysis depends significantly on the spacecraft orbit, particularly whether equatorial or polar. A similar statement also applies to the SKR data as outlined in section 2.4 below. Figure 2 thus provides a summary of relevant orbit characteristics (adapted from Provan et al. (2018)), plotted over the interval 1 January 2016 to 30 September 2017, or equivalently $t = 4{,}383 - 5{,}022$ days as displayed at the bottom of the figure, where $t = 0$ corresponds to 00 UT on 1 January 2004 (essentially the start of the Cassini science mission with remote monitoring of SKR). Year boundaries are shown at the top of the figure together with northern summer solstice on 24 May 2017, corresponding to $t = 4{,}893$ days. Solar latitude peaked at 26.73° at solstice, but varied on either side only between 25.69° at the start of the interval and 26.67° at the end, so that near-solstice conditions prevailed throughout. Cassini revolution (Rev) numbers, defined from apoapsis to apoapsis, are plotted at the times of periapsis at the top of the figure, numbered every 10 Revs. The interval spans from Rev 229 to the last (part) Rev 293, with the F ring orbits corresponding to Revs 251–270 and the proximal orbits to Revs 271–293.

Figure 2a shows the latitude range on each Rev, plotted at periapsis, where the red and blue circles show the latitude of apoapsis and periapsis, respectively. We note that the maximum/minimum latitudes on a given orbit are equal to plus/minus the inclination of the orbit plane to the planet's equator. Figure 2b similarly shows the radial range on each Rev plotted on a log scale, while Figure 2c shows the LT of apoapsis (red) and periapsis (blue), respectively, plotted at their corresponding times. These data show that the orbit was near-equatorial at the start of the interval, but that the inclination to the planetary equator was steadily increased to ~40° by mid-2016 ($t \approx 4{,}600$ days), with apoapsis at ~55 R_S located at maximum northern latitudes near the dawn meridian. (Saturn's 1 bar equatorial radius, R_S, is 60,268 km.) Subsequently, the inclination was increased further to ~60° to the end of mission, while apoapsis and periapsis were moved closer to the equator in the midnight and noon sectors, respectively. Apoapsis was reduced to near ~20 R_S (Titan's orbit), while periapsis was moved sequentially to smaller values ending the mission in Saturn's upper atmosphere near the periapsis of Rev 293.

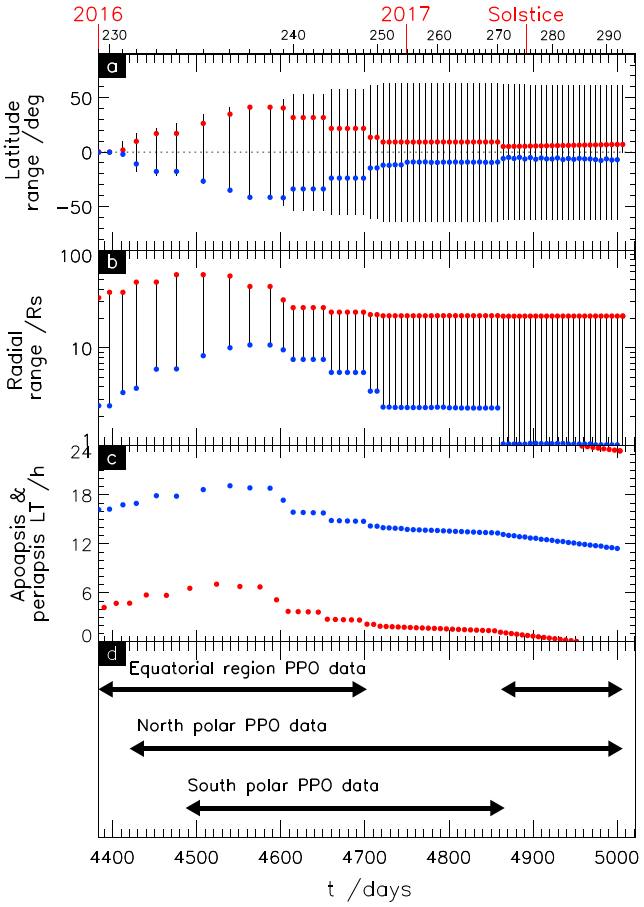

Figure 2. Cassini orbital parameters are shown plotted over the interval 1 January 2016 to 30 September 2017, corresponding to $t = 4{,}383 - 5{,}022$ days as displayed at the bottom of the figure, where $t = 0$ corresponds to 00 UT on 1 January 2004. Year boundaries are shown at the top of the plot, together with northern summer solstice on 24 May 2017 ($t = 4{,}893$ days), and Cassini Rev numbers plotted at the time of periapsis spanning Revs 229–293. Figure 2a shows the latitude range (deg) on each Rev, plotted at the time of periapsis, with the blue and red circles showing the latitudes of periapsis and apoapsis, respectively. Figure 2b shows the radial range on each Rev (R_S) on a log scale, also plotted at the time of periapsis. Figure 2c shows the LTs (hr) of apoapsis (red) and periapsis (blue), plotted at their corresponding times. Figure 2d indicates the consequent nature of the PPO perturbation fields available for analysis, whether the quasi-uniform equatorial field inside the main PPO-related field-aligned current layers (upper arrowed intervals), or the northern or southern quasi-dipolar polar field outside of those current layers (middle and lower arrowed intervals, respectively).

In Figure 2d the arrowed intervals show the nature of the PPO-related magnetic oscillations that these orbits made available for analysis, related either to the quasi-uniform fields of the equatorial magnetosphere (upper arrowed intervals) inside of the main PPO field-aligned currents (see Figures 1b and 1e), or to the northern or southern quasi-dipolar fields on the corresponding polar sides of those current layers (middle and lower arrowed intervals, respectively). It can be seen that initially the near-equatorial orbit allowed observation only of the rotating equatorial quasi-uniform field, but that the subsequently increasing orbit inclination provided access to northern polar data and then also to southern polar data, on inbound and outbound passes, respectively, in the first half of 2016. Equatorial data from near-periapsis passes eventually became unusable for analysis toward the end of 2016, when the pass duration became short compared with the PPO period such that the phase of the modulation could no longer be reasonably accurately determined. While northern polar data then remained available to the end of mission, the change in orbit between the F ring and proximal Revs exchanged southern polar data for southern equatorial region data on outbound passes. With regard to SKR emissions, observation of northern dawnside sources was favored during the first half of the interval due to the predawn northerly moderate latitude of apoapsis where the spacecraft spent most time. Northern and southern sources were more evenly favored in terms of latitude in the second half of the interval, however, in particular during the F ring and proximal Revs, as apoapsis moved toward the equator.

2.3. Magnetic Field Data Analysis Procedures

Analysis of the magnetic data begins by fitting the rotating function given by

$$B_i = B_{i0}\cos\left(\Phi_g(t) - \varphi - \psi_i\right) \tag{1}$$

to selected "quiet" intervals of suitably filtered residual field data, from which the planetary field has been subtracted. Here φ is azimuth with respect to the planetary rotation/magnetic axis measured from noon increasing in the sense of planetary rotation, $\Phi_g(t)$ is a guide phase corresponding to an oscillation close in period to that of the data, taken for simplicity to be of a fixed period τ_g such that

$$\Phi_g(t) = \frac{360t}{\tau_g}, \tag{2}$$

where we again take $t = 0$ at 00 UT on 1 January 2004, and the fit parameters for spherical polar field component $i = (r, \theta, \varphi)$ are the amplitude B_{i0} and the relative phase ψ_i (modulo 360°). We note that the analysis of Provan et al. (2018) also takes account of downtail radial propagation effects at distances beyond ~12 R_S, but these effects are small for the present data set. While the relative phase ψ_r of the r component is employed as measured, the phases of the θ and φ components are rotated to "agree" with that of the r component according to Figure 1, in phase or antiphase for θ for southern or northern PPO system data, respectively, and lagging or leading quadrature for φ for equatorial or polar data, respectively, before being combined together (see Provan et al. (2018) for full details). Phases are not available from all field components for all Revs, however, due, for example, to variations associated with ring current crossings contributing power to the filter band in equatorial data, or to proximity to the main PPO field-aligned currents that separate the quasi-uniform from the quasi-dipolar fields in higher-latitude data. Running linear fits are then made to the remaining Rev-by-Rev relative phase values to define the northern and southern system phases $\psi_{N,S}(t)$ relative to the guide phase, such that the magnetic PPO phases $\Phi_{N,S}(t)$ are given by

$$\Phi_{N,S}(t) = \Phi_g(t) - \psi_{N,S}(t), \tag{3}$$

defining the azimuth as a function of time where the r component of a given system maximizes, that is, the azimuth with respect to noon of the $\Psi_{N,\,S} = 0^{\circ}$ meridians in Figure 1. The phase fits employed here were derived from running 125-day segments of data computed every 12.5 days (Provan et al., 2018). The corresponding magnetic PPO periods are then obtained by differentiation of the phases

$$\tau_{N,S}(t) = \frac{360}{\left(\frac{d\Phi_{N,S}}{dt}\right)}, \tag{4}$$

where $\Phi_{N,\,S}(t)$ is expressed in degrees.

2.4. SKR Data Analysis Procedures

SKR is emitted predominantly in the extraordinary (X) mode which is right-hand polarized in the northern hemisphere and left-hand polarized in the southern hemisphere, with northern sources illuminating a large region down to −20° latitude in the southern hemisphere, and southern sources similarly illuminating the region to +20° latitude in the northern hemisphere, outside of a shadow zone extending to ~4 R_S in the equatorial plane (Kimura et al., 2013; Lamy, Zarka, Cecconi, Hesse, et al., 2008; Lamy, Zarka, Cecconi, Prangé, et al., 2008). Emissions from a given hemisphere may thus be selected either by latitude separation of the data, or by sense of polarization, or both, with the polarization technique allowing separation of data near ±20° of the equator where emissions from both hemispheric sources can be observed simultaneously. In previous analyses (e.g., Lamy, 2011), the hemispheric origin of the SKR emissions was determined principally by using polarization-separated data, limited to latitudes above −20° for northern emissions, and to latitudes below +20° for southern emissions. During the present interval, however, the signal-to-noise ratio of these principally high-latitude data (Figure 2a) was improved by use of the total SKR signal (i.e., not separated by polarization state, meaning that the right-hand and left-hand data are summed together), but separated by latitude limits of +10° for the northern data and −10° for the southern data, these limits being applied over the whole interval for the southern data, and after t = 4,562 days in mid-2016 for the northern data, prior to which the previous polarization separation method was employed (Lamy, 2017). For further discussion of SKR data and analysis procedures the reader is referred, for example, to Lamy et al. (2009, 2011).

Following this separation of the northern and southern SKR emissions, the data were transposed into power time series by integrating the 100–500-kHz spectral band. The lower limit on this band excludes contributions from lower frequency narrowband emissions, while the upper limit was chosen both for consistency with previous related studies and because higher-frequency SKR emissions, that is, up to ~1 MHz, do not display PPO modulations as clearly as those in the chosen band. The power time series were then Lomb-Scargle analyzed to form normalized periodograms from the logarithm of the normalized integrated powers (Lamy, 2011, 2017). As in previous studies, the periodograms employed here were derived using running 200-day data segments computed at 1-day intervals. The SKR PPO periods, $\tau^{*}_{N,S}$, are determined by tracking long-lived near-continuous peaks in the periodograms derived from the data associated with northern and southern emissions, respectively. A complicating feature is the presence in some data intervals of dual modulation, that is, the presence in data selected for one hemisphere of modulations at the period associated with the other (Lamy, 2011). This is indeed a feature of the SKR data during the present interval (Lamy, 2017), as will be addressed in section 4. The SKR phases $\Phi^{*}_{N,S}(t)$ are then defined by integration of the SKR periods via an expression analogous to equation (4), and referenced by sinusoidally fitting the average power as a function of phase and defining SKR maxima at $\Phi^{*}_{N,S}(t) = 360^{\circ}L$ for successive integers L. With this definition we note that the (modulo 360°) difference between the magnetic and SKR phases for a given system, defined as

$$\Delta\Phi^{*}_{N,S}(t) = \Phi_{N,S}(t) - \Phi^{*}_{N,S}(t), \tag{5}$$

then gives the azimuth with respect to noon of the northern and southern systems at times of corresponding SKR maxima, that is, the azimuth of the $\Psi_{N,\,S} = 0^{\circ}$ meridians at $\Phi^{*}_{N,S}(t) = 0^{\circ}$ modulo 360°.

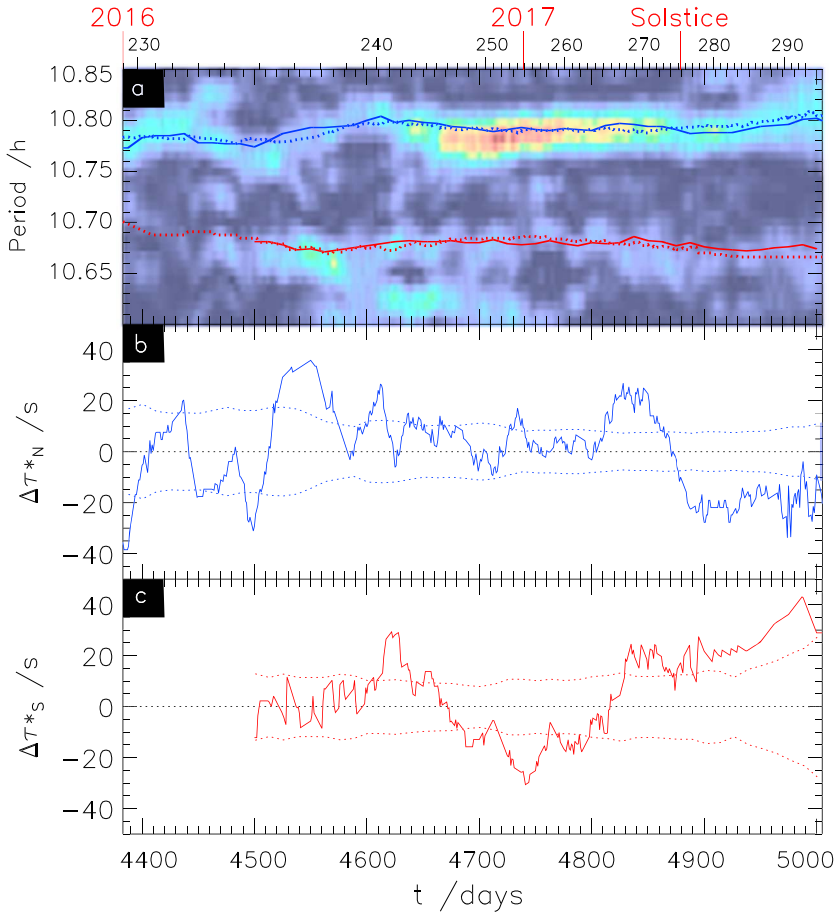

Figure 3. Plot over the same interval as Figure 2 showing a comparison of the northern (blue) and southern (red) PPO periods deduced from SKR emission and magnetic field data. Figure 3a shows a color-coded normalized Lomb-Scargle periodogram of the total SKR power over the interval, on which the SKR periods deduced by Lamy (2017) are superposed (dotted lines) following near-continuous maxima, together with the periods deduced from the magnetic phase data shown in Figure 4 (solid lines). Figures 3b and 3c show the differences between these determinations for the northern and southern periods, respectively, where specifically we show the magnetic minus the SKR periods. The blue and red dotted lines in these plots indicate the mean expected differences due to uncorrelated uncertainties in these determinations if the uncertainties in the SKR values are the same as those derived by Provan et al. (2018) for the magnetic data, hence $\sqrt{2}$ times the latter values.

3. Results

3.1. Comparison of Magnetic Field and SKR PPO Periods

In Figure 3 we provide a comparison of the PPO periods derived directly by Lomb-Scargle analysis of the SKR measurements by Lamy (2017) and from the gradient of the magnetic phase measurements by Provan et al. (2018) as described above. A comparison of the phases will be presented in section 3.2. Figure 3a shows for simplicity a color-coded periodogram of the total SKR emission over the same interval as in Figure 2, where all the SKR data have been included irrespective of latitude and polarization, thus including emissions from both hemispheres. The derived PPO periods have been superposed, dotted lines for the northern (blue) and southern (red) SKR periods tracking the periodogram peaks, and similarly colored solid lines for the magnetic periods. We note that the southern magnetic PPO period could not be determined from the generally dual-modulated near-equatorial data prior to $t \approx 4,500$ days due to low southern system amplitudes relative to the northern, but was determined principally from southern polar data thereafter until the interval of proximal orbits (Figure 2d).

It can be seen from Figure 3a that the analyses of the two independent data sets with different methods yield closely similar periods over the whole interval, typically varying by no more than ±0.01 hr (i.e., ±36 s

corresponding to ~ ±0.1%) about 10.79 hr for the northern system and 10.68 hr for the southern. These values are very close to those attained by mid-2015 after the interval of period coalescence at 10.66 hr between mid-2013 and mid-2014 and subsequent period reversal (Provan et al., 2016; Ye et al., 2016). Consistent with these results, Carbary et al. (2017) have also reported energetic electron modulations during the F ring and proximal orbit intervals with a near-constant period of 10.79 ± 0.01 hr, as observed most clearly in northern hemisphere data. However, they did not detect the southern system period in either southern or northern hemisphere electron data.

In Figures 3b and 3c we examine the differences in period between the two data sets for the northern and southern systems, respectively, defined as $\Delta\tau^*_{N,S} = \tau_{N,S} - \tau^*_{N,S}$, that is, the magnetic period minus the SKR period, and we first consider the magnitude of possible systematic differences. As mentioned in section 1, systematic differences can occur between the magnetic field and SKR periods during intervals in which the LT of apoapsis, where the spacecraft spends most time, changes rapidly. This may change the LT of the SKR sources to which the measurements are sensitive and consequently the relative phasing between the magnetic field and the SKR modulations, thus leading to small but systematic differences in derived periods. Period differences due to this effect during typical Cassini orbit evolutions have been estimated theoretically by Andrews et al. (2011) to be ~10–20 s, consistent with directly measured values determined by Provan et al. (2014). During the interval investigated here, the LT of spacecraft apoapsis changed from the dawn to the midnight sector (Figure 2c), but as we show in section 3.2, the relative phasing of the modulations remained approximately fixed throughout. Correspondingly, there is no evidence of significant systematic period differences being present during the interval, apart possibly from the final interval when increased uncertainty estimates and differences occur due to the declining amount of data within the running analysis intervals. Excluding the data after 4,950 days, the mean magnetic-SKR period differences are found to be +2.2 and +3.3 s for the northern and southern PPO systems, respectively, corresponding to uncertainties in phase of only ~30° over ~500 days. Such values are at the limit of resolution of these analyses (Provan et al., 2018).

Having shown that the systematic differences are very small, we now consider the random differences associated with uncertainties in the two period determinations. Provan et al. (2018) provided estimates of the magnetic field period uncertainties that arise from the fits to the phase data, depending on the length of the data interval, the fit variance (essentially the mean square deviation of the phase points from the fitted line), and the number of phase data points included in the fit (Cowley & Provan, 2016). Values are plotted in Figure S3d in the supporting information of Provan et al. (2018), lying typically in the range ~5–15 s, with an averaged value over the interval of ~9 s. This corresponds to an uncertainty in phase of ~25° over the 125-day fit intervals employed. Conservative formal uncertainties in the SKR periods are given by the full width at half maximum (FWHM) of the peaks in the Lomb-Scargle periodograms, depending principally on the length of the data interval employed. These values are typically rather larger than the magnetic field uncertainties at ~0.01 hr (~36 s), as may be judged, for example, from the width of the peaks in the periodogram in Figure 3a. More precisely, for intervals with well-defined periods such as $t = 4{,}715 - 4{,}950$ days for the northern emissions, and $t = 4{,}750 - 4{,}770$ and $t = 4{,}800 - 4{,}890$ days for the southern emissions, the mean FWHMs are found to be 0.0108 hr (39 s) for the northern data, and 0.0128 hr (46 s) for the southern data. For uncorrelated uncertainties, the differences between the two independent period determinations should be given by the quadratic sum of the contributing uncertainties, that is, the square root of the sum of the squares of the two values, ~10 s for the magnetic values and ~40 s for the SKR values. However, the difference values in Figures 3b and 3c are seen to vary typically in the range ~ ±20 s, with mean values of the absolute differences over the interval of 12.9 and 13.0 s for the northern and southern systems, respectively. While these empirical differences are compatible with the estimated uncertainties in the magnetic period values, they also suggest that the effective uncertainties in the SKR periods are a little smaller than the conservative FWHM estimates, and similar in magnitude to the magnetic period uncertainties. For example, assuming equal ~9 s contributions to the total error gives a combined uncertainty in the overall differences of $\tilde{}\sqrt{2}\times 9 \approx 13$ s, as found in Figure 3. We note that a similar result was previously obtained by Provan et al. (2014) in comparisons of postequinox magnetic field and SKR period data in the interval 2011–2013. The blue dotted lines in Figure 3b and the red dotted lines in Figure 3c show estimated uncertainty values that are $\sqrt{2}$ times the magnetic period uncertainties in Figure S3d of Provan et al. (2018), corresponding to the quadratic sum of equal but uncorrelated errors. These values appear to provide an adequate account of the mean differences in period determined from the independent analyses.

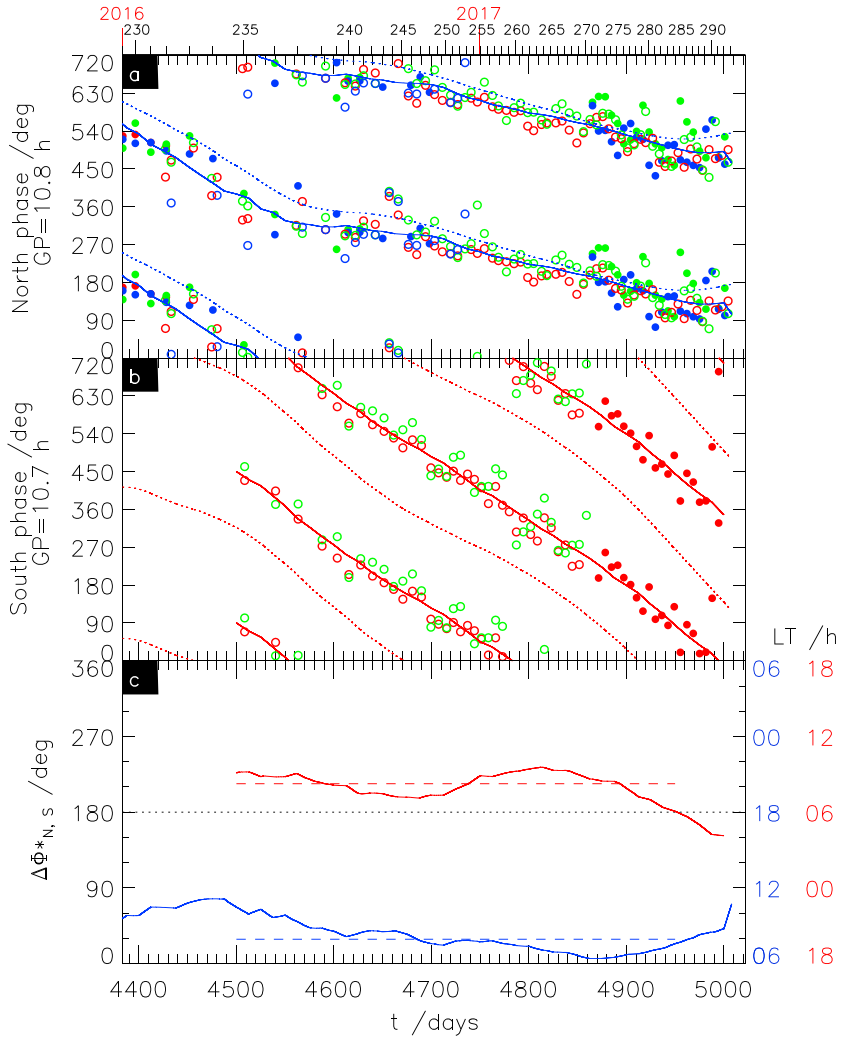

Figure 4. Plots over the same interval and in a format related to Figure 3 showing a comparison of the northern (blue) and southern (red) magnetic field and SKR PPO phases. Figure 4a shows the northern magnetic field (solid line) and SKR (dotted line) phases relative to a guide phase with guide period 10.8 hr, specifically $\psi_N(t)$ in equation (3) and analogously $\psi^*_N(t)$, where circles show the Rev-by-Rev magnetic field phase values from which the magnetic phase model was derived (see text for further details). Figure 4b similarly shows the southern magnetic field (solid line) and SKR (dotted line) phases relative to a guide phase with guide period 10.7 hr, specifically $\psi_S(t)$ in equation (3) and analogously $\psi^*_S(t)$, where circles again show the Rev-by-Rev phase values from which the magnetic phase model was derived. Figure 4c shows the differences between the magnetic and SKR phases for the northern (blue) and southern (red) systems, $\Delta\Phi^*_{N,S} = \Phi_{N,S} - \Phi^*_{N,S} = \psi^*_{N,S} - \psi_{N,S}$, giving the azimuth with respect to noon of the quasi-uniform equatorial fields of the two systems (i.e., the azimuths of the $\Psi_{N,\,S} = 0^\circ$ meridians) at corresponding SKR maxima. The mean values over the common interval of southern and northern data (4,500–4,950 days) are shown by the red and blue dashed lines, respectively. The LT of the centers of the upward field-aligned currents of the northern (blue) and southern (red) systems according to Figures 1b and 1e, respectively, are indicated on the right.

3.2. Comparison of Magnetic Field and SKR PPO Phases

Figure 4 compares the PPO phases derived from the magnetic and SKR data over the same interval as Figures 2 and 3. In Figures 4a and 4b we plot the Rev-by-Rev magnetic phase values ψ_i from equation (1) used to define the phases of the northern and southern PPO systems, respectively, relative to a guide phase given by equation (2) with guide periods of 10.8 and 10.7 hr, respectively. Two cycles of phase are shown on the vertical axes to aid visualization of data continuity, with each data point being plotted twice. The northern and southern polar data (open circles) are thus shown in Figures 4a and 4b, respectively, while the dual-modulated equatorial data is (in general) plotted in both panels (solid circles), in northern and southern

formats in Figures 4a and 4b, respectively. As described in section 2.3, the phases of the *r* component (red) are plotted as measured, while those of the θ (green) and φ (blue) have been rotated to "agree" with that of the *r* component according to physical regime as indicated by the diagrams in Figures 1c and 1f. The blue and red solid lines in Figures 4a and 4b show the northern and southern magnetic phases $\psi_{N,S}(t)$ in equation (3), respectively, relative to these guide phases, derived from running 125-day linear fits to the phase data, with a cadence of 12.5 days (Provan et al., 2018). The slowly falling values indicate rotation periods slightly smaller than the guide periods employed, as already seen in Figure 3a. The blue and red dotted lines show the northern and southern SKR phase models $\psi^*_{N,S}(t)$ relative to the same guide phases, defined analogously to equation (3), derived by integration of the SKR periods as described in section 2.4. It can be seen that to a first approximation the magnetic and SKR phases are in phase for the northern system, and in antiphase for the southern.

In Figure 4c we show the difference between the northern (blue) and southern (red) magnetic and SKR phases as defined by equation (5) (i.e., $\Delta\Phi^*_{N,S} = \Phi_{N,S} - \Phi^*_{N,S} = \psi^*_{N,S} - \psi_{N,S}$), which we recall from section 2.4 gives the azimuth with respect to noon of the $\Psi_{N,S} = 0^\circ$ meridians at the times of corresponding northern and southern SKR maxima. Excluding the data beyond 4,950 days for the reason given in section 3.2, the mean value for the southern system is $\Delta\Phi^*_S \approx 214^\circ$, while over the same interval (of southern data availability), the mean value for the northern system is $\Delta\Phi^*_N \approx 29^\circ$, close to a difference of 180°. These values are marked in the figure by the red and blue dashed lines, respectively. Over the whole interval of the study up to 4,950 days the mean northern value is a little larger at $\Delta\Phi^*_N \approx 37^\circ$. These phase differences thus show that over the interval of joint northern and southern data availability up to 4,950 days, the quasi-uniform field of the northern system on average pointed radially outward at ~14.3 hr LT in the postnoon sector at the times of northern SKR maxima, while the quasi-uniform field of the southern system pointed essentially opposite to ~2.5 hr LT in the postmidnight sector at the times of southern SKR maxima. The ranges about these values are seen in Figure 4 to be ~ ±2 hr LT. Such results are typical of those obtained earlier in the Cassini mission when apoapsis also lay on the dawnside of the planet (Andrews et al., 2008, 2012; Provan et al., 2014, 2016). The implication for both systems is that at the times of corresponding SKR maxima the main upward currents, centered near $\Psi_N = 90^\circ$ for the northern system (Figure 1b) and near $\Psi_S = 270^\circ$ for the southern system (Figure 1e), were both located at ~8.5 hr LT in the dawn-to-noon sector, suggesting a related location of the SKR sources. Equivalent scales of LT for the centers of the upward currents at corresponding SKR maxima of the northern (blue) and southern (red) systems are shown on the right side of Figure 4c.

4. Dual Modulation of SKR Emissions

Lamy (2017) reported that the southern SKR periodogram displays a secondary peak at the northern period after late 2016, spanning northern summer solstice, this mirroring the situation observed during southern summer conditions in 2005–2007 when a secondary peak occurred in the northern periodogram at the southern period. During the southern summer interval the magnetic field data show that the southern PPO system was stronger than the northern with a north/south amplitude ratio ~0.4 (Andrews et al., 2012), while at least during the later (F ring and proximal orbit) part of the interval examined here the northern system has been found to be stronger than the southern with a south/north amplitude ratio of ~0.7 (Hunt, Provan, Bunce, et al., 2018; Hunt, Provan, Cowley, et al., 2018; Provan et al., 2018). The secondary peak thus occurs in the periodogram derived from the data selected for the weaker system, at the period of the stronger system.

Dual modulation in SKR data was also present during the immediate postequinox interval ~2010–2012 when the two magnetic field amplitudes became highly variable, changing abruptly between southern dominant, northern dominant, and near-equal amplitudes at ~100–200-day intervals (Provan et al., 2013). This dual modulation resulted in some ambiguity in interpretation of the periods observed in the SKR data, leading to a few apparent conflicts with the results derived from magnetic field data (Cowley & Provan, 2015, 2016; Fischer et al., 2014, 2015). The purpose of the discussion here, however, is not to reopen this minor controversy, but to point out that the dual modulations discussed by Fischer et al. (2014, 2015) were reported as being locked in phase with each other. That is to say, the modulations in SKR power at a given period,

apparently emitted from opposite hemispheres as indicated by their polarization, occurred in phase with each other.

One possible physical explanation for dual modulation lies in the interhemispheric closure of the main PPO-related field-aligned currents as depicted in Figures 1b and 1e, it being known that approximately half of the main current closes cross-field in the magnetosphere, and half in the opposite hemisphere (Bradley et al., 2018; Hunt et al., 2015). However, assuming that the spacecraft is primarily responding to SKR sources at similar LTs in the two hemispheres, it is evident that this should produce approximate antiphase modulations, since when the PPO current is directed upward in a given sector in one hemisphere, enhancing the acceleration of auroral electrons and the consequent emissions, it is directed downward in the other. Enhancement of the upward current and auroral electron acceleration in the opposite hemisphere would then occur one-half cycle later, in antiphase with the generating hemisphere. This antiphase condition is indeed the phasing of the interhemispheric response observed in auroral UV emissions by Bader et al. (2018). On the other hand, Kivelson and Jia (2018) have argued that the auroral acceleration process is at least partly bidirectional in nature, resulting not only in downward acceleration toward the ionosphere but also in upward acceleration to form beams that travel along auroral field lines to produce emissions in the opposite hemisphere. Previous studies have shown that the main PPO-related field-aligned currents of the northern and southern systems are co-located on the same outer magnetospheric closed field lines as each other (Bradley et al., 2018; Hunt et al., 2014, 2015). In this case, therefore, the dual modulations at a given period would occur in phase with each other, as implied by the findings of Fischer et al. (2014, 2015). We therefore now examine the relative phasing of the SKR modulations in the northern and southern emissions during the northern summer interval studied here.

Figure 5 shows gray-scaled plots of the logged SKR powers, selected as described in section 2.4 following Lamy (2017), plotted versus time on the horizontal axes and modulo 360° SKR phase on the vertical axes, where two cycles of phase and repeated data are shown to aid visualization of the modulations at the PPO periods. Figure 5a shows the northern power plotted versus northern SKR phase, while Figure 5c shows the southern power plotted versus southern SKR phase. In both cases modulations of the power with maxima at 0°/360° are evident essentially throughout. To the right of each of the gray-scaled data panels in Figures 5b and 5d we plot averaged values versus SKR phase on the same vertical scale, where the green and purple lines show averages over the first and second parts of the interval, respectively, split specifically at $t = 4{,}700$ days (late 2016), while the black line shows the average over the whole interval. We note that the first half interval contains data from Revs 229–248 during which the orbit inclination was steadily increased from the equatorial plane to ~60° with apoapsis at significantly high northern latitudes (Figure 2a) favoring observation of northern SKR sources, while the second half contains data from Revs 249–293 (essentially the F ring and proximal orbits) during which the inclination remained near-constant with apoapsis near the equatorial plane, providing similar temporal coverage of northern and southern SKR emissions up to high latitudes. All these averaged profiles, of the northern power with respect to the northern phase, and the southern power with respect to the southern phase, are seen to peak close to phases 0°/360°, as expected from the construction of the SKR phase models outlined in section 2.4.

Dual modulation of these SKR powers would result in additional banding in the gray-scaled plots, falling in phase with time in the northern data in Figure 5a and rising in phase with time in the southern data in Figure 5c. Maxima would lie along the red dotted lines in Figure 5a and along the blue dotted lines in Figure 5c if the SKR modulations from the two hemispheres are in phase. Such banding is clearly seen to be present in the southern data in Figure 5c, particularly in the central part of the interval, but is not visually evident in the northern data in Figure 5a, in line with the results presented by Lamy (2017). In Figures 5e–5h we plot the northern power data versus southern SKR phase and the southern power data versus northern SKR phase, in the same format as Figures 5a–5d. Although the primary power banding in these plots is evidently that of the main hemispheric modulation, with bands rising in phase in Figure 5e (following the blue dotted lines in Figures 5c) and falling in phase in Figure 5g (following the red dotted lines in Figures 5a), modulation of the southern power with the northern SKR phase is clearly present in the gray-scaled plot in Figure 5g with maxima lying near 0°/360° over much of the interval. The averaged values in Figure 5h show similar modulation to the northern power versus northern phase in Figure 5b, but with lesser overall power from the southern sources. Modulation of the southern SKR at the northern period is thus approximately in

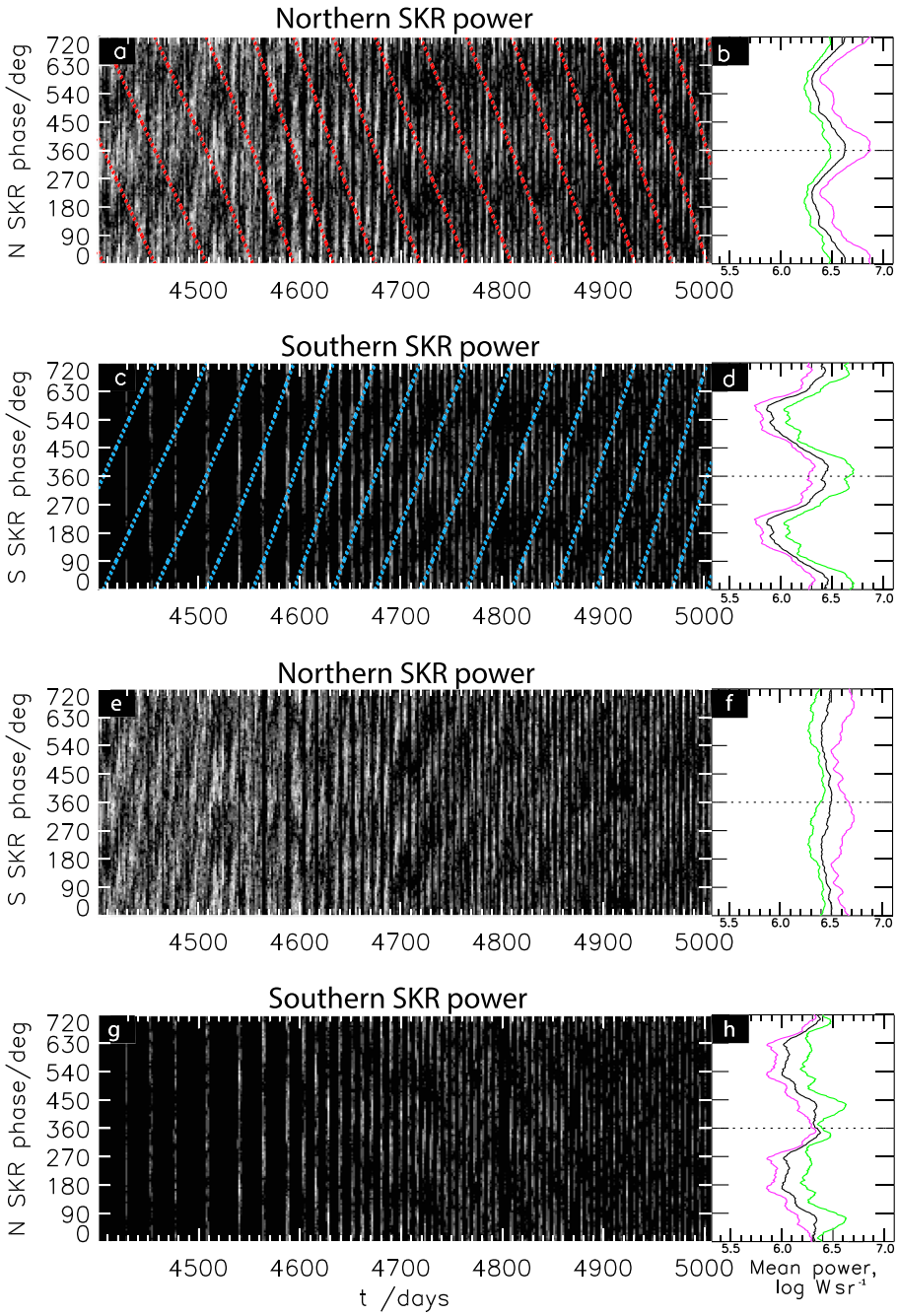

Figure 5. Gray scaled logged SKR powers, selected following Lamy (2017) as described in section 2.4, are shown plotted versus time on the horizontal axes over the same interval as in Figures 2–4, and versus SKR phase on the vertical axes where two cycles of phase and repeated data are shown. On the right of each gray-scaled panel we show the logged powers plotted similarly versus phase on the vertical axis, averaged over the intervals $t \leq 4{,}700$ days (green), $t \geq 4{,}700$ days (purple, essentially encompassing the F ring and proximal Revs), and the whole interval (black). Figures 5a and 5b show plots of the northern SKR power versus northern SKR phase, with red dotted lines in the gray-scaled panel showing where power peaks would lie if modulated in phase with the southern SKR system. Figures 5c and 5d show plots of the southern SKR power versus southern SKR phase, with blue dotted lines in the gray-scaled panel showing where power peaks would lie if modulated in phase with the northern SKR system. Figures 5e and 5f show the northern SKR power similarly plotted versus southern SKR phase, while Figures 5g and 5h show the southern SKR power plotted versus northern SKR phase.

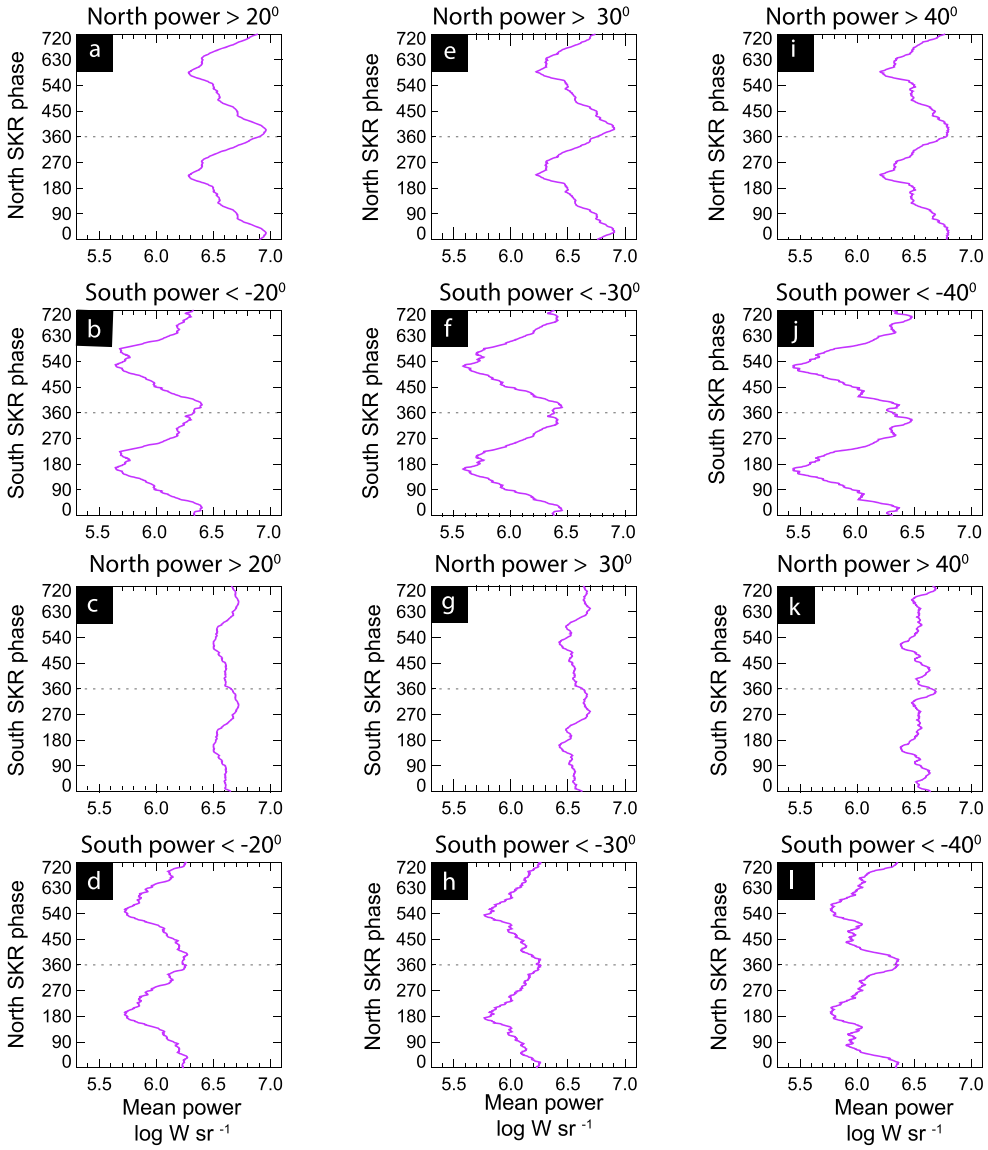

Figure 6. Total logged SKR power averaged over the interval for $t \geq 4,700$ days (essentially the F ring and proximal Revs) plotted versus SKR phase, in the same format as the plots on the right side of Figure 5, but with differing limits on the latitudinal data coverage as indicated in the plot labels. Specifically, the limits are above +20° for the northern data and below −20° for the southern data in Figures 6a–6d, above +30° for the northern data and below −30° for the southern data in Figures 6e–6h, and above +40° for the northern data and below −40° for the southern data in Figures 6i–6l.

phase with the corresponding modulation of the northern SKR. Modulation of the northern SKR at the southern period in Figures 5e and 5f is evidently much weaker, however, with peaks that shift in phase between the first half interval (green) and the second half interval (purple), from which it is hard to draw firm conclusions.

As indicated in section 2.4, following Lamy (2017) the SKR powers in Figure 5 were for the most part obtained using a > +10° latitude limit for the northern data (after 4,562 days) and a < −10° latitude limit for the southern data, these limits usually being sufficient to separate emissions from northern and southern hemispheric sources (Gurnett et al., 2009; Kimura et al., 2013; Lamy, Zarka, Cecconi, Hesse, et al., 2008). However, this limit is near the edge of the shadow zone from a given hemisphere, leading to possible concern that the observed dual modulation might instead be due to imperfect elimination of emissions originating from the opposite hemisphere. We have therefore repeated the analysis using more restrictive latitude

cutoffs, further restricting the analysis to the second part of the data interval ($t \geq 4{,}700$ days, essentially the F ring and proximal Revs) for which the latitude coverage remained approximately fixed with comparable temporal coverage of both northern and southern emissions (Figure 2a). Results are presented in Figure 6, where we show only the averaged power profiles versus northern and southern SKR phases in the same vertical order as in Figure 5, with results restricting the data to increasingly large latitudes being shown in the three figure columns from left to right. Specifically, the limits are ±20° in Figures 6a–6d, ±30° in Figures 6e–6h, and ±40° in Figures 6i–6l.

For the southern SKR power the same basic pattern of in phase modulation at the northern period is present at all three levels of latitude cutoff in Figures 6d, 6h, and 6l, though with increased levels of fluctuation present in Figure 6l. Modulation in the northern power at the southern period remains weak, though with some indication of approximate in phase modulation in Figures 6c and 6g. Overall, however, these results principally demonstrate that the in phase modulation of the southern emissions at the northern period persists in SKR data obtained at high southern latitudes well outside of the ±20° shadow zone, thus confirming their southern origin, rather than being due, for example, to imperfect elimination of emissions originating from the opposite hemisphere. Again, the in phase nature of the dual modulation is not consistent with the effect of interhemispheric closure of the main PPO-related field-aligned current flow, as is the case for UV emissions (Bader et al., 2018), and may instead be due to bidirectional acceleration of auroral electrons as proposed by Kivelson and Jia (2018). An alternative possibility is electron acceleration related to secondary PPO currents of reversed sign flowing in the opposite hemisphere (see, e.g., Provan et al., 2018), although why in this case the secondary currents produce a larger effect than that of the oppositely directed primary currents remains an open question.

5. Summary and Conclusions

We have examined the relationships between the periods and phases of Saturn's PPOs determined from magnetic field oscillation data by Provan et al. (2018) and from modulated SKR emissions by Lamy (2017), over the last ~600 days of the Cassini mission from the beginning of 2016 to end of mission in mid-September 2017. This interval is of particular importance since magnetic data from the brief near-periapsis segments of the orbits during the second half of the interval, not used in the present analysis, provide unique information on PPO phenomena in regions not previously accessed during the mission, in particular on field lines threading through and inside the rings on the final proximal orbits. Our principal findings are as follows.

1. Both data sets are consistent with essentially unchanging periods over the interval, ~10.79 hr for the northern and ~10.68 hr for the southern, typically varying about these values by no more than ±0.01 hr. Seasonal conditions were near constant throughout, essentially those of northern solstice which occurred toward the end of the interval. The periods are close to those attained by mid-2015 after period coalescence at ~10.66 hr between mid-2013 and mid-2014 and subsequent reversal, with the northern period becoming enduringly longer than the southern for the first time during the Cassini era.
2. The mean absolute differences between the two independently derived periods over the interval are ~13 s (0.0036 hr) for both northern and southern periods. These values are consistent with the ~9-s uncertainties in the magnetic field values estimated by Provan et al. (2018), and suggest that the uncertainties in the SKR values are similar in magnitude, a little smaller than the conservative uncertainties derived from the FWHM of the Lomb-Scargle periodograms.
3. The mean differences in magnetic and SKR periods over the whole interval are ~2 s (0.0006 hr) for the northern system and ~3 s (0.0009 hr) for the southern system, at the limit of resolution. Thus, no measureable systematic differences between the derived magnetic and SKR periods were present, which might have been due, for example, to changes in the LT of the SKR sources to which the data primarily responded.
4. Correspondingly, the relative phasing between the magnetic oscillations and the SKR modulations is only weakly and slowly varying over the interval, as the LT of apoapsis, where the spacecraft spends most time, varied from near dawn to near midnight. The quasi-uniform equatorial perturbation field of the northern PPO system pointed radially outward consistently between ~12 and 16 hr LT at northern

SKR maxima, on average at ~14.3 hr LT over the interval of joint magnetic northern and southern system data, while the related perturbation field of the southern PPO system pointed oppositely between ~0 and 4 hr LT, on average at ~2.5 hr LT, at southern SKR maxima. Given the expected relationship between the PPO perturbation fields and field-aligned currents (Figure 1), these orientations are such that the upward currents of both systems were located in the postdawn sector between ~6 and 10 hr LT, typically at ~8.5 hr LT, at the times of corresponding SKR maxima. These findings are in agreement with previous analyses of data obtained when spacecraft apoapsides were located in the dawnside sector (Andrews et al., 2008, 2012; Provan et al., 2014, 2016).

5. We confirm the result of Lamy (2017) that the weaker southern SKR emissions are dual modulated at both northern and southern PPO periods, mirroring conditions during 2005–2007 when the weaker northern emissions were found to be dual modulated at both PPO periods. We have shown that dual modulation occurs consistently in SKR data increasingly restricted to lie at southern latitudes greater than limits from 10° to 40°, that is, from the edge of the expected northern shadow zone to well within the shadow zone, indicating that the northern period modulation originates from southern sources rather than being due to imperfect elimination of northern sources.
6. Modulation of the southern emissions at the northern PPO period is found to be approximately in phase with the corresponding modulations in the northern hemisphere. In phase modulations are opposite to expectations for the direct effect of interhemispheric current flow, for which approximate antiphase modulations in the two hemispheres are anticipated as found in UV auroral data (Bader et al., 2018), but are consistent with the bidirectional auroral electron acceleration picture proposed recently by Kivelson and Jia (2018). Alternatively, such emissions could be associated with secondary PPO-related currents of reversed sense flowing in the opposite hemisphere.

Acknowledgments
Work at the University of Leicester was supported by STFC grant ST/N000749/1. L.L. was supported by the CNES. E.J. B. was supported by a Royal Society Wolfson Research Merit Award. We thank S. Kellock and the Cassini magnetometer team at Imperial College for the access to processed magnetic field data. Calibrated magnetic field and radio data from the Cassini mission are available from the NASA Planetary Data System at the Jet Propulsion Laboratory (https://pds.jpl.nasa.gov/).

References

Andrews, D. J., Bunce, E. J., Cowley, S. W. H., Dougherty, M. K., Provan, G., & Southwood, D. J. (2008). Planetary period oscillations in Saturn's magnetosphere: Phase relation of equatorial magnetic field oscillations and SKR modulation. *Journal of Geophysical Research*, *113*, A09205. https://doi.org/10.1029/2007JA012937

Andrews, D. J., Cecconi, B., Cowley, S. W. H., Dougherty, M. K., Lamy, L., Provan, G., & Zarka, P. (2011). Planetary period oscillations in Saturn's magnetosphere: Evidence in magnetic field phase data for rotational modulation of Saturn kilometric radiation emissions. *Journal of Geophysical Research*, *116*, A09206. https://doi.org/10.1029/2011JA016636

Andrews, D. J., Coates, A. J., Cowley, S. W. H., Dougherty, M. K., Lamy, L., Provan, G., & Zarka, P. (2010). Magnetospheric period oscillations at Saturn: Comparison of equatorial and high-latitude magnetic field periods with north and south SKR periods. *Journal of Geophysical Research*, *115*, A12252. https://doi.org/10.1029/2010JA015666

Andrews, D. J., Cowley, S. W. H., Dougherty, M. K., Lamy, L., Provan, G., & Southwood, D. J. (2012). Planetary period oscillations in Saturn's magnetosphere: Evolution of magnetic oscillation properties from southern summer to post-equinox. *Journal of Geophysical Research*, *117*, A04224. https://doi.org/10.1029/2011JA017444

Andrews, D. J., Cowley, S. W. H., Dougherty, M. K., & Provan, G. (2010). Magnetic field oscillations near the planetary period in Saturn's equatorial magnetosphere: Variation of amplitude and phase with radial distance and local time. *Journal of Geophysical Research*, *115*, A04212. https://doi.org/10.1029/2007JA014729

Bader, A., Badman, S. V., Kinrade, J., Cowley, S. W. H., Provan, G., & Pryor, W. R. (2018). Statistical planetary period oscillation signatures in Saturn's UV auroral intensity. *Journal of Geophysical Research: Space Physics*, *123*, 8459–8472. https://doi.org/10.1029/2018JA025855

Bradley, T. J., Cowley, S. W. H., Provan, G., Hunt, G. J., Bunce, E. J., Wharton, S. J., et al. (2018). Field-aligned currents in Saturn's nightside magnetosphere: Subcorotation and planetary period oscillation components during northern spring. *Journal of Geophysical Research: Space Physics*, *123*, 3602–3636. https://doi.org/10.1002/2017JA024885

Burton, M. E., Dougherty, M. K., & Russell, C. T. (2010). Saturn's internal planetary magnetic field. *Geophysical Research Letters*, *37*, L24105. https://doi.org/10.1029/2010GL045148

Carbary, J. F., & Mitchell, D. G. (2013). Periodicities in the Saturn's magnetosphere. *Reviews of Geophysics*, *51*, 1–30. https://doi.org/10.1002/rog.20006

Carbary, J. F., Mitchell, D. G., Kollman, P., Krupp, N., & Roussos, E. (2017). Energetic electron periodicities during the Cassini grand finale. *Journal of Geophysical Research: Space Physics*, *122*, 12,229–12,235. https://doi.org/10.1002/2017JA024836

Cowley, S. W. H., & Provan, G. (2015). Planetary period oscillations in Saturn's magnetosphere: Comments on the relation between post-equinox periods determined from magnetic field and SKR emission data. *Annales Geophysicae*, *33*(7), 901–912. https://doi.org/10.5194/angeo-33-901-2015.

Cowley, S. W. H., & Provan, G. (2016). Planetary period oscillations in Saturn's magnetosphere: Further comments on the relationship between post-equinox properties deduced from magnetic field and Saturn kilometric radiation measurements. *Icarus*, *272*, 258–276. https://doi.org/10.1016/j.icarus.2016.02.051

Cowley, S. W. H., Zarka, P., Provan, G., Lamy, L., & Andrews, D. J. (2016). Comment on "A new approach to Saturn's periodicities" by J. F. Carbary. *Journal of Geophysical Research: Space Physics*, *121*, 2418–2422. https://doi.org/10.1002/2015JA021996

Dougherty, M. K., Cao, H., Khurana, K. K., Hunt, G. J., Provan, G., Kellock, S., et al. (2018). Saturn's magnetic field revealed by Cassini's grand finale. *Science*, *362*(6410), eaat5434. https://doi.org/10.1126/science.aat5434

Fischer, G., Gurnett, D. A., Kurth, W. S., Ye, S.-Y., & Groene, J. B. (2015). Saturn kilometric radiation periodicity after equinox. *Icarus*, *254*, 72–91. https://doi.org/10.1016/j.icarus.2015.03.014

Fischer, G., Ye, S.-Y., Groene, J. B., Ingersoll, A. P., Sayanagi, K. M., Menietti, J. D., et al. (2014). A possible influence of the great white spot on Saturn kilometric radiation periodicity. *Annales Geophysicae*, *32*(12), 1463–1476. https://doi.org/10.5194/angeo-32-1463-2014

Galopeau, P. H. M., & Lecacheux, A. (2000). Variations of Saturn's radio rotation period measured at kilometer wavelengths. *Journal of Geophysical Research*, *105*(A6), 13,089–13,101. https://doi.org/10.1029/1999JA005089

Gurnett, D. A., Groene, J. B., Averkamp, T. F., Kurth, W. S., Ye, S.-Y., & Fischer, G. (2011). The SLS4 longitude system based on a tracking filter analysis of the rotational modulation of Saturn kilometric radiation. In H. O. Rucker, W. S. Kurth, P. Louarn, & G. Fischer (Eds.), *Planetary Radio Emissions VII* (pp. 51–64). Vienna: Austrian Academy of Science Press.

Gurnett, D. A., Groene, J. B., Persoon, A. M., Menietti, J. D., Ye, S.-Y., Kurth, W. S., et al. (2010). The reversal of the rotational modulation rates of the north and south components of Saturn kilometric radiation near equinox. *Geophysical Research Letters*, *37*, L24101. https://doi.org/10.1029/2010GL045796

Gurnett, D. A., Kurth, W. S., Hospodarsky, G. B., Persoon, A. M., Averkamp, T. F., Cecconi, B., et al. (2005). Radio and plasma wave observations at Saturn from Cassini's approach and first orbit. *Science*, *307*(5713), 1255–1259. https://doi.org/10.1126/science.1105356

Gurnett, D. A., Lecacheux, A., Kurth, W. S., Persoon, A. M., Groene, J. B., Lamy, L., et al. (2009). Discovery of a north-south asymmetry in Saturn's radio rotation period. *Geophysical Research Letters*, *36*, L16102. https://doi.org/10.1029/2009GL039621

Hunt, G. J., Cowley, S. W. H., Provan, G., Bunce, E. J., Alexeev, I. I., Belenkaya, E. S., et al. (2014). Field-aligned currents in Saturn's southern nightside magnetosphere: Sub-corotation and planetary period oscillation components. *Journal of Geophysical Research: Space Physics*, *119*, 9847–9899. https://doi.org/10.1002/2014JA020506

Hunt, G. J., Cowley, S. W. H., Provan, G., Bunce, E. J., Alexeev, I. I., Belenkaya, E. S., et al. (2015). Field-aligned currents in Saturn's northern nightside magnetosphere: Evidence for inter-hemispheric current flow associated with planetary period oscillations. *Journal of Geophysical Research: Space Physics*, *120*, 7552–7584. https://doi.org/10.1002/2015JA021454

Hunt, G. J., Provan, G., Bunce, E. J., Cowley, S. W. H., Dougherty, M. K., & Southwood, D. J. (2018). Field-aligned currents in Saturn's magnetosphere: Observations from the *F*-ring orbits. *Journal of Geophysical Research: Space Physics*, *123*, 3806–3821. https://doi.org/10.1002/2017JA025067

Hunt, G. J., Provan, G., Cowley, S. W. H., Dougherty, M. K., & Southwood, D. J. (2018). Planetary period oscillations during the closest approach of Cassini's ring grazing orbits. *Geophysical Research Letters*, *45*, 4692–4700. https://doi.org/10.1002/2018GL077925

Jia, X., & Kivelson, M. G. (2012). Driving Saturn's magnetospheric periodicities from the upper atmosphere/ionosphere: Magnetotail response to dual sources. *Journal of Geophysical Research*, *117*, A11219. https://doi.org/10.1029/2012JA018183

Jia, X., Kivelson, M. G., & Gombosi, T. I. (2012). Driving Saturn's magnetospheric periodicities from the upper atmosphere/ionosphere. *Journal of Geophysical Research*, *117*, A04215. https://doi.org/10.1029/2011JA017367

Kimura, T., Lamy, L., Tao, C., Badman, S. V., Kasahara, S., Cecconi, B., et al. (2013). Long-term modulations of Saturn's auroral radio emissions by the solar wind and seasonal variations controlled by the solar ultraviolet flux. *Journal of Geophysical Research: Space Physics*, *118*, 7019–7035. https://doi.org/10.1002/2013JA018833

Kivelson, M. G., & Jia, X. (2018). Coupled SKR emissions in Saturn's northern and southern ionospheres. *Geophysical Research Letters*, *45*, 2893–2900. https://doi.org/10.1002/2017GL075425

Kurth, W. S., Averkamp, T. F., Gurnett, D. A., Groene, J. B., & Lecacheux, A. (2008). An update to a Saturnian longitude system based on kilometric radio emissions. *Journal of Geophysical Research*, *113*, A05222. https://doi.org/10.1029/2007JA012861

Lamy, L. (2011). Variability of southern and northern SKR periodicities. In H. O. Rucker, W. S. Kurth, P. Louarn, & G. Fischer (Eds.), *Planetary Radio Emissions VII* (pp. 39–50). Vienna: Austrian Academy of Science Press.

Lamy, L. (2017). The Saturnian kilometric radiation before the Cassini grand finale. In G. Fischer, G. Mann, M. Panchenko, & P. Zarka (Eds.), *Planetary Radio Emissions VIII* (pp. 171–190). Vienna: Austrian Academy of Science Press.

Lamy, L., Cecconi, B., Prangé, R., Zarka, P., Nichols, J. D., & Clarke, J. T. (2009). An auroral oval at the footprint of Saturn's kilometric radio sources, co-located with the UV aurorae. *Journal of Geophysical Research*, *114*, A10212. https://doi.org/10.1029/2009JA014401

Lamy, L., Cecconi, B., Zarka, P., Canu, P., Schippers, P., Kurth, W. S., et al. (2011). Emission and propagation of Saturn kilometric radiation: Magnetoionic modes, beaming pattern, and polarization state. *Journal of Geophysical Research*, *116*, A04212. https://doi.org/10.1029/2010JA016195

Lamy, L., Zarka, P., Cecconi, B., Hesse, S., & Prangé, R. (2008). Modeling of Saturn kilometric radiation arcs and equatorial shadow zone. *Journal of Geophysical Research*, *113*, A10213. https://doi.org/10.1029/2008JA013464

Lamy, L., Zarka, P., Cecconi, B., Prangé, R., Kurth, W. S., & Gurnett, D. A. (2008). Saturn kilometric radiation: Average and statistical properties. *Journal of Geophysical Research*, *113*, A07201. https://doi.org/10.1029/2007JA012900

Lecacheux, A., Galopeau, P., & Aubier, M. (1997). Re-visiting Saturn kilometric radiation with Ulysses/URAP. In H. O. Rucker, S. J. Bauer, & A. Lecacheux (Eds.), *Planetary Radio Emissions IV* (pp. 313–326). Vienna: Austrian Academy of Science Press.

Provan, G., Andrews, D. J., Arridge, C. S., Cowley, S. W. H., Milan, S. E., Dougherty, M. K., & Wright, D. M. (2009). Polarization and phase of planetary period oscillations on high latitude field lines in Saturn's magnetosphere. *Journal of Geophysical Research*, *114*, A02225. https://doi.org/10.1029/2008JA013782

Provan, G., Andrews, D. J., Cecconi, B., Cowley, S. W. H., Dougherty, M. K., Lamy, L., & Zarka, P. (2011). Magnetospheric period magnetic field oscillations at Saturn: Equatorial phase "jitter" produced by superposition of southern- and northern-period oscillations. *Journal of Geophysical Research*, *116*, A04225. https://doi.org/10.1029/2010JA016213

Provan, G., Cowley, S. W. H., Bradley, T. J., Bunce, E. J., Hunt, G. J., & Dougherty, M. K. (2018). Planetary period oscillations in Saturn's magnetosphere: Cassini magnetic field observations over the northern summer solstice interval. *Journal of Geophysical Research: Space Physics*, *123*, 3859–3899. https://doi.org/10.1002/2018JA025237

Provan, G., Cowley, S. W. H., Lamy, L., Bunce, E. J., Hunt, G. J., Zarka, P., & Dougherty, M. K. (2016). Planetary period oscillations in Saturn's magnetosphere: Coalescence and reversal of northern and southern periods in late northern spring. *Journal of Geophysical Research: Space Physics*, *121*, 9829–9862. https://doi.org/10.1002/2016JA023056

Provan, G., Cowley, S. W. H., Sandhu, J., Andrews, D. J., & Dougherty, M. K. (2013). Planetary period magnetic field oscillations in Saturn's magnetosphere: Post-equinox abrupt non-monotonic transitions to northern system dominance. *Journal of Geophysical Research: Space Physics*, *118*, 3243–3264. https://doi.org/10.1002/jgra.50186

Provan, G., Lamy, L., Cowley, S. W. H., & Dougherty, M. K. (2014). Planetary period oscillations in Saturn's magnetosphere: Comparison of magnetic oscillations and SKR modulations in the post-equinox interval. *Journal of Geophysical Research: Space Physics*, *119*, 7380–7401. https://doi.org/10.1002/2014JA020011

Smith, C. G. A. (2006). Periodic modulation of gas giant magnetospheres by the neutral upper atmosphere. *Annales Geophysicae*, *24*(10), 2709–2717. https://doi.org/10.5194/angeo-24-2709-2006

Smith, C. G. A., Ray, L. C., & Achilleos, N. A. (2016). A planetary wave model for Saturn's 10.7-h periodicities. *Icarus*, *268*, 76–88. https://doi.org/10.1016/j.icarus.2015.12.041

Ye, S.-Y., Fischer, G., Kurth, W. S., Menietti, J. D., & Gurnett, D. A. (2016). Rotational modulation of Saturn's radio emissions after equinox. *Journal of Geophysical Research: Space Physics*, *121*, 11,714–11,728. https://doi.org/10.1002/2016JA023281